28. Umamaheswari, R., Ramach, S. and Nobi, E. P., Mapping the extend of seagrass meadows of Gulf of Mannar Biosphere Reserve, India using IRS ID satellite imagery. *Int. J. Biodiver. Conserv.*, 2009, **1**(5), 187–193.
29. Das, H. S., Status of seagrass habitats of the Andaman and Nicobar coast. Technical Report 4, Salim Ali Centre for Ornithology and Natural History (SACON), Coimbatore, India, 1996.
30. Thangaradjou, T., Sivakumar, K., Nobi, E. P. and Dilipan, E., Distribution of seagrasses along the Andaman and Nicobar Islands: a post tsunami survey. In *Recent Trends in Biodiversity of Andaman and Nicobar Islands*, Zoological Survey of India, Kolkata, 2010, Chapter 11, pp. 157–160.
31. Savurirajan, M., Equbal, J., Lakra, R. K., Satyam, K. and Thiruchitrambalam, G., Species diversity and distribution of seagrasses from the South Andaman, Andaman and Nicobar Islands, India. *Bot. Mar.*, 2018, **61**(3), 225–234.
32. Paulose, N. E., Dilipan, E. and Thangaradjou, T., Integrating Indian remote sensing multi-spectral satellite and field data to estimate seagrass cover change in the Andaman and Nicobar Islands, India. *Ocean Sci. J.*, 2013, **48**(2), 173–181.
33. Dsouza, E. and Patankar, V., First underwater sighting and preliminary behavioural observations of Dugongs (*Dugong dugon*) in the wild from Indian waters, Andaman Islands. *J. Threatened Taxa*, 2009, **1**(1), 49–53.
34. NITI Aayog Report, Transforming the Islands through Creativity and Innovation, 2019.
35. Island wise – Area and Population, Census 2011.
36. Sen2Cor Configuration and User Manual, Ref. S2-PDGS-MPC-L2A-SUM- V2.5.5 (European Space Agency), 2018.
37. Qasim, S. Z. and Ansari, Z. A., Food components of the Andaman Sea, *Indian J. Marine Sci*., 1981, **10**(3), 276–279.
38. D'Souza, E., Patankar, V., Arthur, R., Marbà, N. and Alcoverro, T., Seagrass herbivory levels sustain site-fidelity in a remnant dugong population. *PLoS ONE*, 2015, **10**(10), e0141224.
39. Waycott, M., Duarte, C. M., Carruthers, T. J., Orth, R. J., Dennison, W. C., Olyarnik, S. and Kendrick, G. A., Accelerating loss of seagrasses across the globe threatens coastal ecosystems. *Proc. Natl. Acad. Sci.*, 2009, **106**(30), 12377–12381.
40. Short, F. T., Polidoro, B., Livingstone, S. R., Carpenter, K. E., Bandeira, S., Bujang, J. S. and Erftemeijer, P. L., Extinction risk assessment of the world's seagrass species. *Biol. Conserv.*, 2011, **144**(7), 1961–1971.
41. Sridhar, R., Thangaradjou, T., Kannan, L. and Astalakshmi, S., Assessment of coastal bio-resources of the Palk Bay, India, using IRS-LISS-III data. *J. Indian Soc. Remote Sensing*, 2010, **38**(3), 565–575.

ACKNOWLEDGEMENTS. We thank CAMPA Authority of the Ministry of Environment, Forest and Climate Change, Government of India for funding this study. We would like to thank CSSTEAP, Director (CSSTEAP) and Director (IIRS) for their support and facilities. We thank the State Forest Department of Andaman and Nicobar Islands and Prasad Gaidhani for support during field work. We are grateful to Director, Wildlife Institute of India and Director, Indian Institute of Remote Sensing for their constant encouragement.

Received 9 September 2019; revised accepted 3 January 2020

doi: 10.18520/cs/v118/i8/1275-1282

Development of wind speed retrieval model using RISAT-1 SAR cross-polarized observations

Jagdish Prajapati[1,2,]*, Abhisek Chakraborty[1], Bipasha Paul Shukla[1] and Raj Kumar[1]

[1]Earth, Ocean, Atmosphere, Planetary Sciences and Applications Area,
Space Applications Centre, Indian Space Research Organisation,
Ahmedabad 380 015, India
[2]Department of Mathematics, Gujarat University,
Ahmedabad 380 009, India

In this study, a method for retrieving ocean surface wind speed using C-band cross-polarization SAR observations has been outlined. A linear least square technique has been used to develop a Geophysical Model Function (GMF), C2P. The GMF was derived using NRCS observations from RISAT-1 and wind-speed observations from ASCAT. The correlation between observed and simulated NRCS values obtained from C2P was 0.66, with a negative bias of 0.01 dB and the corresponding root mean square difference of 1.13 dB. Subsequently, the developed GMF was tested with 774 RISAT-1 MRS datasets to retrieve wind speed along the Indian coast and also of the tropical cyclone 'Megh'. The measured intensity and radius of maximum wind speed were 30 m s^{-1} and 16.65 km respectively. Subsequently, the retrieved wind speed was validated with ASCAT wind-speed observations. The statistical comparison of RISAT-1 and ASCAT observed wind speed showed negative biases of 0.90 and 0.34 m s^{-1} with the corresponding RMSD of 2.11 and 1.77 m s^{-1} respectively, for CMOD5.N and C2P. The developed GMF C2P showed 16% more accuracy than that of CMOD5.N.

Keywords: Cross-polarization, geophysical model function, ocean surface, wind speed retrieval.

OCEAN surface winds are highly important for numerical weather and ocean state forecasting, study of oceanic transportation and processes occurring at the air–sea interface. For the last four decades, ocean surface vector winds at synoptic scales are operationally being retrieved from spaceborne scatterometers. Such observations of ocean surface winds are assimilated in numerical models for improving operational forecasts at moderate resolution. Scatterometer-based observations are available with coarser spatial resolution in the range 12–50 km with wider data gaps in the coastal regions. However, wind intensity of cyclones computed using Ku-band scatterometer data tends to underestimate the actual scenario. Therefore, in extreme conditions like cyclones, backscattered power received by microwave scatterometers mainly

---

*For correspondence. (e-mail: jagdish.aug1991@gmail.com)

working in the Ku-band saturates under high-wind conditions. Also because of coarser resolution of scatterometer data, distribution of cyclonic wind patterns in different quadrants cannot be precisely estimated. Such information is highly desired for estimation of cyclone tracks.

To this end, Synthetic Aperture Radar (SAR) working in the microwave spectrum of electromagnetic waves provides a unique opportunity of retrieving ocean surface winds with very high (~few metres) spatial resolution. Because of narrower footprints than a scatterometer, SAR-derived winds are also available in the coastal regions with good accuracy. A SAR payload working in the C-band with co- (VV or HH) or cross- (VH or HV) polarization mode accurately measures backscattered energy from wind-generated capillary-gravity wave through Bragg's scattering mechanism. Under extreme weather conditions, the C-band cross-polarized backscattered power shows linear relationship with winds over oceans. Such backscattered power does not depend on wind direction and incidence angle of SAR. This enables us to retrieve ocean surface wind speed from cross-polarized C-band SAR under moderate to high-wind conditions with reasonably good accuracy[1,2]. Several researchers have shown the potential of cross-polarized SAR sensors in retrieving ocean winds under high wind conditions[3–6]. In addition, co-pol Geophysical Model Functions (GMFs) saturate at high wind speed[7,8], while cross-pol GMFs show linear response[9,10]. In this study, we develop an empirical C-band Cross-Polarized (C2P) model for backscattered power from RISAT-1 launched by the Indian Space Research Organization (ISRO).

RISAT-1 is a C-band SAR. Data collected by the satellite in coastal regions can be used to fill the information gap in scatterometry. Since RISAT-1 operates in the microwave spectrum, it is not obscured by extensive cloud cover. It can provide data during day and night under all-weather condition. The choice of operation of C-band RISAT-1 SAR in single, dual and circular polarizations is useful in flood and crop monitoring, generic vegetation, forestry, soil moisture, geology, sea ice, coastal processes and cyclonic storms[11]. Also, imaging of the Earth's surface is possible in different modes; HRS, FRS-1, FRS-2, MRS and CRS with swath widths ranging from 30 to 220 km (ref. 11). Here we focus on VH and HV cross-pol measurements in ScanSAR mode, collocated with ASCAT (Advanced Scatterometer of European Space Agency) observations from the Physical Oceanography Distributed Active Archive Center, Jet Propulsion Laboratory, Pasadena, California. After radiometric calibration[12], all HV and VH cross-pol RISAT-1 SAR image pixels were downscaled to 1 km × 1 km using re-gridding through spatial averaging. In order to avoid interference and land contamination, we have used only those values of wind speed and normalized radar cross section (NRCS) which are 10 km away in the ocean from the shoreline. For collocation purpose, a temporal window of 90 min was maintained between the scatterometer and SAR observations. Totally 308 RISAT-1 SAR images in MRS mode with dual polarization (HH + HV) were collected along the Indian coastline. Data were processed for collocation, which resulted in 886 match-up points of RISAT-1 cross-pol observations. Linear least square was used to obtain wind-retrieval model. A C-band GMF, C2P at cross-polarization was used to retrieve high wind speed from RISAT-1 SAR data, which was independent of radar incidence angle[5]. When compared to the single polarization (HH or VV) observation, cross-pol (VH or HV) observation was better in measuring ocean roughness with different scattering characteristics, with a scope to retrieve cyclone wind speed. There were 187 collocated points with wind speeds above 15 m s^{-1} and the highest wind speed was 20.08 m s^{-1} (Figure 1). Figure 1 shows the relation between RISAT-1 and ASCAT-measured cross-pol NRCS and wind speed (U_{10}) respectively. Cross-pol NRCS does not depend on incidence angle or wind direction, but depends on wind speed[13]. Therefore we can derive a model relating NRCS of cross-pol (σ^0) to wind speed (U_{10}).

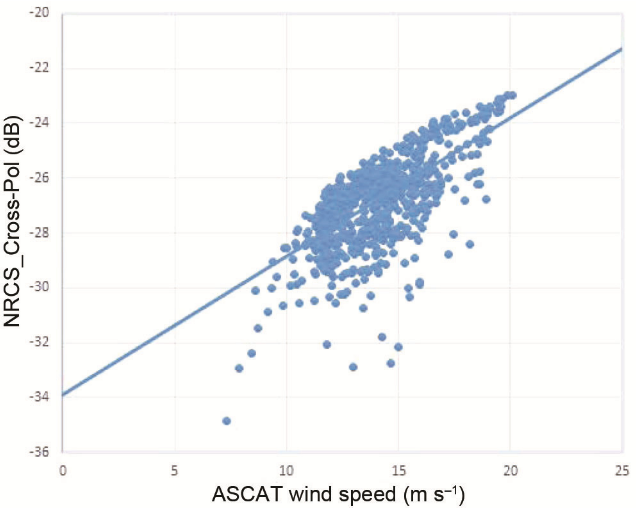

Figure 1. Observed normalized radar cross section (NRCS) from Radar Imaging Satellite-1 versus measured wind speed from advanced scatterometer.

GMF is the mathematical equation between wind speed and backscattering coefficient (σ^0). Here we use the dataset $((U_{10})_p, (\sigma^0)_p)$, where p is the number of observations. The equation of the desired GMF may be assumed to the linear and is given below as

$$\sigma^0 = a * U_{10} + b. \quad (1)$$

The vector of n residuals f_p is given by the following equation

$$f_p = (\sigma^0)_p - (a * (U_{10})_p + b),\ p = 1, 2, \ldots, n.$$

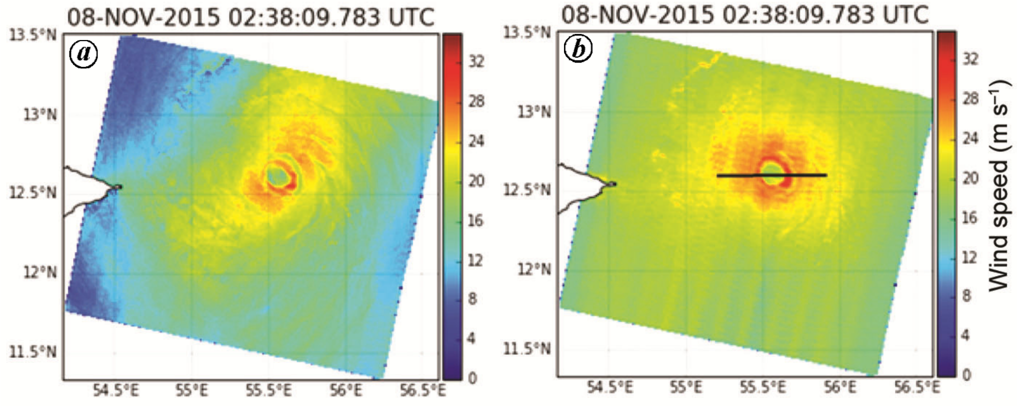

Figure 2. Wind speed of cyclone Megh using (***a***) CMOD5.N and (***b***) C-band cross-polarized model.

Sum of the squares of f_ps is given by

$$F=\sum_{p=1}^{n}[(\sigma^0)_p-(a*(U_{10})_p+b)]^2.$$

Since σ^0 and U_{10} are known, *a* and *b* are parameters of the function *F*. The minimization equation for function *F* is given as

$$\frac{\partial F}{\partial a}=\frac{\partial F}{\partial b}=0. \tag{2}$$

The above condition, i.e. eq. (2), yields

$$a\sum_{p=1}^{n}((U_{10})_p)^2+b\sum_{p=1}^{n}(U_{10})_p=\sum_{p=1}^{n}(U_{10})_p(\sigma^0)_p,$$

$$a\sum_{p=1}^{n}(U_{10})_p+nb=\sum_{p=1}^{n}(\sigma^0)_p.$$

Solution of the above simultaneous equations gives the value of *a* and *b*. Hence, the required equation of GMF using eq (1) is computed as follows

$$\sigma^0=0.504*U_{10}-33.884, \tag{3}$$

where σ^0 and U_{10} are in dB and m s^{-1} respectively. The correlation coefficient of observed σ^0 and simulated σ_m^0 with eq. (3) is 0.66, with a negative bias and the corresponding root mean square difference (RMSD) of 0.01 and 1.13 dB respectively. The GMF does not contain any terms related to incidence angle, i.e. it is not dependent on incidence angle. Thus, we have developed a C-band GMF (C2P) for retrieving wind speed at C-band cross-pol observation. To retrieve ocean surface wind speed, we have constructed a cost function as given below

$$Z(k,l)=\frac{[\sigma_s^0(k,l)-\sigma^0(k,l)]^2}{\nabla\sigma}+\frac{[u(k,l)-spd(k,l)]^2}{\nabla u}, \tag{4}$$

where σ_s^0 and σ^0 are the simulated and observed cross-pol NRCS respectively, *u* is the model wind speed and *spd* is the trial wind speed in the range 0–50 ms^{-1}. *k* and *l* define the location of the pixel in the SAR image, i.e. *k* and *l* represent the row and column number of the pixel. Model speeds are taken from the atmospheric model ECMWF. In order to find the optimum solution of wind speed, we have minimized the cost function for every pixel of the SAR image using variational inversion method[14]. The wind speeds derived from CMOD5.N and C2P are validated against ASCAT[11].

Figure 2 *a* and *b* shows RISAT-1 retrieved wind speed of cyclone 'Megh' in VV and VH polarization on 8 November 2015 at 02 : 38 UTC. The cyclone intensity was 30.0 and 28.3 m s^{-1} with C2P and CMOD5.N respectively. Figure 3 *a* and *b* shows the optimum solution of wind speed obtained through minimization of cost function. Wind speeds retrieved through CMOD5.N and C2P were validated against ASCAT data. Statistical results show negative biases of 0.90 and 0.43 m s^{-1} with the corresponding RMSD of 2.11 and 1.77 m s^{-1} respectively (Table 1), for CMOD5.N and C2P, which is well within the acceptable limits[15]. Further, we have analysed wind speed profile of the cyclone along an arbitrary transect (black line in Figure 2 *b*). Figure 4 shows the wind speed profile along the transect. The intensity and radius of maximum wind measured from the centre are 30.0 m s^{-1} and 16.65 km.

A wind retrieval model for moderate as well high wind speeds (pertaining to cyclonic conditions) has been developed using C-band cross polarization of RISAT-1 SAR. The developed GMF relates the ocean surface wind speed to the normalized radar cross-section C-band cross-pol. The co-pol and cross-pol GMFs are employed to construct a cost function for obtaining optimum solution

Table 1. Statistical comparison of wind speeds between Radar Imaging Satellite-1 and Advanced Scatterometer of European Space Agency with CMOD5.N and C-band cross-polarized (C2P) model

Geophysical model functions	Number of points	Bias (m s^{-1})	Root mean square difference (m s^{-1})	STD (m s^{-1})
CMOD5.N	7421	–0.90	2.11	1.61
C2P	7294	–0.43	1.77	1.72

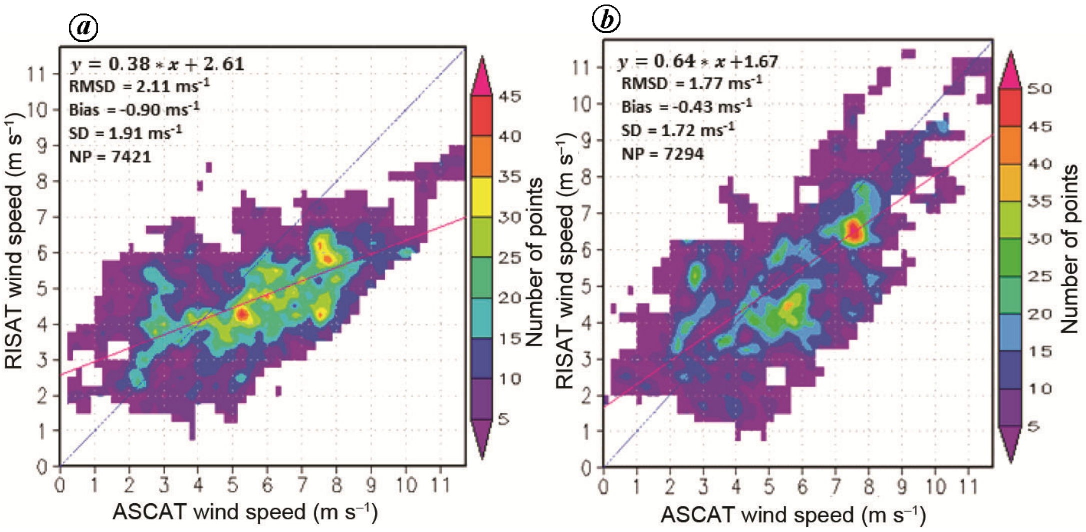

Figure 3. Density scatter plot showing statistical comparison of RISAT-1 retrieved wind speed with ASCAT using (***a***) CMOD5.N and (***b***) C2P.

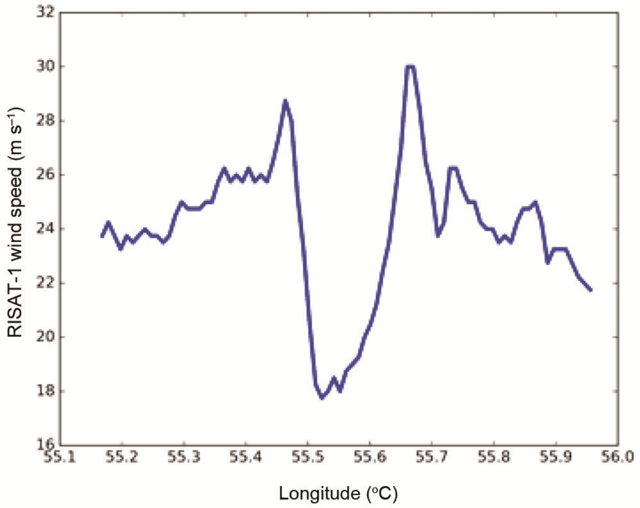

Figure 4. Variation in wind speed along the transect passing through the eye of the cyclone.

of wind speed. In the present study, it has been observed that the existing C-band GMF CMOD5.N is dependent on incidence angle and saturates under high wind speed. Thus, it is unable to generate high wind speeds during tropical cyclones. The developed GMF C2P is independent of incidence angle and does not saturate during high wind speed. Hence, it is better suited to generate high wind speed, as seen in the case of tropical cyclones. The developed GMF C2P shows 16% more accuracy than that of the CMOD5.N. Further, a case study on cyclone Megh was carried out, which demonstrate the greater potential of the developed GMF for cyclones compared to the existing GMF. The main source of error in the quality of retrieved winds from RISAT-1 SAR can be attributed to the accuracy of the radiometric calibration of SAR-derived NRCS. This has been tackled using the standard deviation (the so-called noise parameters) of the observed NRCS in the cost function used for minimizing the simulated versus observed NRCS values[15]. In future, we expect to further improve and establish the accuracy of wind speed retrieval by considering more RISAT-1 SAR images for fine-tuning and validation.

---

1. Zhang, B., Perrie, W. and He, Y., Wind speed retrieval from RADARSAT-2 quad-polarization images using a new polarization ratio model. *J. Geophys. Res.*, 2011, **116**, C08008, doi:10.1029/2010JC006522.
2. Zhang, B. and Perrie, W., Cross-polarized synthetic aperture radar: a new potential technique for hurricanes. *Bull. Am. Meteorol. Soc.*, 2012, **93**, 531–541; doi:10.1175/BAMS-D-11-00001.1.
3. Horstmann, J., Thompson, D. R., Monaldo, F., Iris, S. and Graber, H. C., Can synthetic aperture radars be used to estimate hurricane force winds? *Geophys. Res. Lett.*, 2005, **32**(2), L22801-1–L22801-5.

4. Shen, H., Perrie, W. and He, Y., A new hurricane wind retrieval algorithm for SAR images. *Geophys. Res. Lett.*, 2006, **33**(21), L21812-1–L21812-5.
5. Vachon, P. W. and Wolfe, J., C-band cross-polarization wind speed retrieval. *IEEE Geosci. Remote Sensing Lett.*, 2011, **8**(3), 456–459.
6. Hwang, P. A., Zhang, B. and Perrie, W., Depolarized radar return for breaking wave measurement and hurricane wind retrieval. *Geophys. Res. Lett.*, 2010, **37**(1), L01604-1–L01604-4.
7. Monaldo, F. M., Jackson, C. and Li, X., On the use of Sentinel-1 cross-polarization imagery for wind speed retrieval. *Int. Geosci. Remote Sensing Symp.*, 2017, 392–395.
8. Shao, W. *et al.*, Development of wind speed retrieval from cross-polarization Chinese Gaofen-3 synthetic aperture radar in typhoons. *Sensors*, 2018, **18**, 412.
9. Gao, Y. *et al.,* A wind speed retrieval model for Sentinel-1A EW mode cross-polarization images. *Remote Sensing*, 2019, **11**, 153; doi:10.3390/rs11020153.
10. Mouche, A. *et al.*, Copolarized and cross-polarized SAR measurements for high-resolution description of major hurricane wind structures: application to Irma category 5 hurricane. *J. Geophys. Res. Oceans*, 2019, **124**, 3905–3922; https://doi.org/10.1029/2019JC015056.
11. Jagdish *et al.*, An interesting case of persistent rain cells observed by RISAT-1 SAR over the Indian Ocean during a pair of depression–cyclone interactions (August, 2012). *Remote Sensing Lett.*, 2019, **10**(6), 545–552; doi:10.1080/2150704X.2019.1579377.
12. Jagdish *et al.*, Atmospheric fronts using RISAT-1 SAR data: case studies for shear lines. *IEEE J. Sel. Top. Appl. Earth Observ. Remote Sensing*, 2018, **11**(12), 4711–4717; doi:10.1109/JSTARS.2018.2878753.
13. Zhang, B. *et al.*, Tropical cyclone vector winds from C-band dual-polarization synthetic aperture radar. *Int. Geosci. Remote Sensing Symp.*, 2014, 3522–3525.
14. Jiang, Z. *et al.*, A damped Newton variational inversion method for SAR wind retrieval. *J. Geophys. Res.*, 2016, **122**(2), 823–845.
15. Jagdish, Kumar, S. V. V. A., Chakraborty, A. and Kumar, R., Validation of wind speed retrieval from RISAT-1 SAR images of the North Indian Ocean. *Remote Sensing Lett.*, 2018, **9**(5), 421–428; doi:10.1080/2150704X.2018.1430392.

ACKNOWLEDGEMENTS. We thank the Director, Space Applications Centre, ISRO, Ahmedabad for his encouragement. We also thank NRSC and PODAAC for providing RISAT-1 and ASCAT data respectively, and the RISAT-1 data calibration and validation team. We also thank Shri Rakesh R. Bhavsar and Shri. Deba Jyoti Dhar (Space Applications Centre, ISRO, Ahmedabad) for their valuable suggestions.

Received 12 March 2019; revised accepted 25 December 2019

doi: 10.18520/cs/v118/i8/1282-1286

Correlation between Earth tides and the 2008 M_S 8.0 Wenchuan earthquake sequence

Ruyu Yan[1], **Chaodi Xie**[1,2,*], **Xinglin Lei**[3], **Han Zhang**[1], **Rui Jia**[1] **and Jianping Liao**[4]

[1]Geophysics Department, School of Resources and Earth Science, Yunnan University, Kunming 650091, China
[2]State Key Laboratory of Earthquake Dynamics, Institute of Geology, China Earthquake Administration, Beijing 100029, China
[3]Geological Survey of Japan, AIST, Tsukuba 305-8567, Japan
[4]Hunan Provincial Key Laboratory of Shale Gas Resource Utilization, Hunan University of Science and Technology, Xiangtan 411201, China

This study examines the possibility of tidal triggering in the aftershock sequence of the M_S 8.0 Wenchuan earthquake on 12 May 2008. Two methods, the Schuster spectrum and KORRECT (correlation with a rectangular pulse) methods, were used to explore the periodicities of the aftershock sequence. Firstly, we detected the latent periodicities through the Schuster spectrum method; then, we used the KORRECT method to verify and confirm these periodicities. Moreover, the aftershock catalogue was divided into two subsets using 16 km focal depth to discuss the impact of focal depth on tidal triggering. Results show that the aftershocks in the first few days following the mainshock were mainly triggered by semidiurnal and diurnal tides. In the Longmen Shan Thrust Belt, shallow earthquakes were triggered by diurnal tides and deep earthquakes were triggered by semidiurnal tides.

Keywords: Aftershock, earth tides, KORRECT method, schuster spectrum, 2008 M_S 8.0 Wenchuan earthquake.

THE oceans and solid earth are periodically deformed under the forces of celestial bodies (mainly the Sun and the Moon). We usually refer to them as solid tides and ocean tides. Related research indicates that although the variation of the solid tidal stress is 10^3 Pa, which is much smaller than the average stress drop of the earthquake, the rate of accumulation is usually greater than the tectonic stress[1]. Therefore, when the pressure in the focal area is close to the critical level at which the earthquake occurs, the tides may trigger an earthquake. Studying tidal triggering can provide clues to the physical mechanisms that solve fault rupture.

Because stress changes due to the earth's tide can be predicted, some studies have studied the relationship between the earth's tide and aftershocks. Early in 1966, Berg[2] supposed that the unloading of the crust by large ocean tides may be considered a triggering mechanism for the Alaska earthquake of March 1964, and its major aftershocks. Mohler[3] considered that when tidal stress is favourable for motion on the fault plane, notable events

---

*For correspondence. (e-mail: xiecd@ynu.edu.cn)